nature nanotechnology

SUPPLEMENTARY INFORMATION

https://doi.org/10.1038/s41565-020-0684-7

In the format provided by the authors and unedited.

Nanometric square skyrmion lattice in a centrosymmetric tetragonal magnet

Nguyen Duy Khanh[1,11]✉, Taro Nakajima[1,2], Xiuzhen Yu[1], Shang Gao[1,12,13], Kiyou Shibata[1,14], Max Hirschberger[1,3,4], Yuichi Yamasaki[1,5,6], Hajime Sagayama[7], Hironori Nakao[7], Licong Peng[1], Kiyomi Nakajima[1], Rina Takagi[1,3,8], Taka-hisa Arima[1,9], Yoshinori Tokura[1,3,10] and Shinichiro Seki[1,3,6,8]✉

[1]RIKEN Center for Emergent Matter Science (CEMS), Wako, Japan. [2]Institute for Solid State Physics (ISSP), The University of Tokyo, Chiba, Japan. [3]Department of Applied Physics, The University of Tokyo, Tokyo, Japan. [4]Quantum-Phase Electronics Center, The University of Tokyo, Tokyo, Japan. [5]Research and Services Division of Materials Data and Integrated System (MaDIS), National Institute for Materials Science (NIMS), Tsukuba, Japan. [6]PRESTO, Japan Science and Technology Agency (JST), Kawaguchi, Japan. [7]Institute of Materials Structure Science, High Energy Accelerator Research Organization, Tsukuba, Tsukuba, Japan. [8]Institute of Engineering Innovation, The University of Tokyo, Tokyo, Japan. [9]Department of Advanced Materials Science, The University of Tokyo, Kashiwa, Japan. [10]Tokyo College, The University of Tokyo, Tokyo, Japan. [11]Present address: Institute for Solid State Physics (ISSP), The University of Tokyo, Chiba, Japan. [12]Present address: Materials Science & Technology Division, Oak Ridge National Laboratory, Oak Ridge, TN, USA. [13]Present address: Neutron Science Division, Oak Ridge National Laboratory, Oak Ridge, TN, USA. [14]Present address: Institute of Industrial Science, The University of Tokyo, Meguro, Japan. ✉e-mail: khanh.nguyen@riken.jp; seki@ap.t.u-tokyo.ac.jp

Supplementary Information for

Nanometric square skyrmion lattice in a centrosymmetric tetragonal magnet

Nguyen Duy Khanh, Taro Nakajima, Xiuzhen Yu, Shang Gao, Kiyou Shibata, Max Hirschberger, Yuichi Yamasaki, Hajime Sagayama, Hironori Nakao, Licong Peng, Kiyomi Nakajima, Rina Takagi, Taka-hisa Arima, Yoshinori Tokura and Shinichiro Seki

I. Temperature dependence of magnetic susceptibility

Supplementary Fig. 1 shows the temperature dependence of the magnetic susceptibility χ of $GdRu_2Si_2$ acquired for B // [001] (B = 100 Oe). A peak is observed at T_N = 46 K, which indicates the onset of long-range magnetic order. From a linear fit to the inverse magnetic susceptibility ($1/\chi$) between 100 K and 300 K, we obtain the Curie-Weiss temperature θ_{CW} = 43.6 K. The ratio of Neel temperature to Curie-Weiss temperature is $T_N/\theta_{CW} \approx 1.05$, which implies that the geometrical frustration of short-range exchange interactions is not relevant in this tetragonal lattice system.

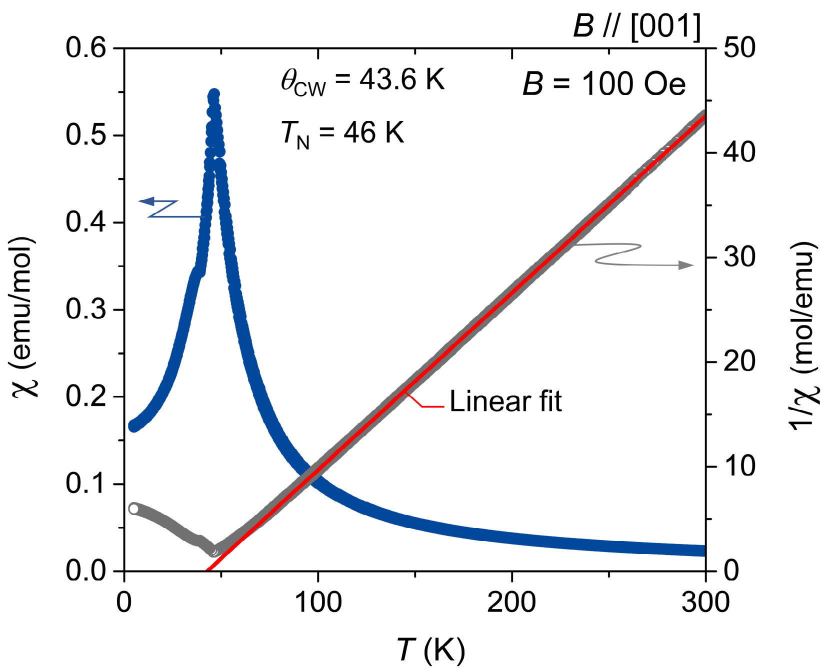

Supplementary Fig. 1 | Temperature dependence of magnetic susceptibility (χ) and inverse magnetic susceptibility ($1/\chi$) for B // [001], measured at 100 Oe.

II. Magnetic structures in Phase I and Phase III

First, we discuss the magnetic structure of Phase III based on the polarized RXS measurement. Supplementary Fig. 2 indicates the intensity profile of magnetic satellite peaks around the fundamental Bragg reflection (4, -2, 0) ± $\boldsymbol{Q}$ at B = 3T, corresponding to phase III, which was obtained in the same experimental geometry as shown in Figure 3. As discussed in the main text, $I_{\pi\text{-}\pi'}$ and $I_{\pi\text{-}\sigma'}$ reflect the [001] and [100] components of $\boldsymbol{m_Q}$, respectively, in this setup. Here, Supplementary Figs. 2a and 2b represent the data for $\boldsymbol{Q_1}$ = (q, 0, 0) and $\boldsymbol{Q_2}$ = (0, q, 0). In both profiles, $I_{\pi\text{-}\pi'}$ is negligibly small, which suggests the absence of a modulated [001] spin component. On the other hand, the observed $I_{\pi\text{-}\sigma'}$ (i.e. [100] component in $\boldsymbol{m_Q}$ profiles for $\boldsymbol{Q_1}$ = (q, 0, 0) and $\boldsymbol{Q_2}$ = (0, q, 0) demonstrate the modulation of an in-plane spin component normal to $\boldsymbol{Q}$. Thus, it can be concluded that the magnetic structure of Phase III is a combination of modulated spin component perpendicular to the direction of $\boldsymbol{Q}$, confined within the tetragonal basal plane, and a field-induced uniform ferromagnetic component parallel to [001] axis, which can be considered as a fan-like structure, as shown in Supplementary Fig. 2e.

Note that the data obtained in Phase I (i.e. Fig. 3c and e in the main text) have a secondary peak located at δ = 0.226, in addition to the main peak located at δ = 0.220 in (4, -2+δ, 0) scan. The selection rule and the δ-value of the former peak are found to be the same as those observed for the magnetic reflection in Phase III (Supplementary Fig. 2). Here, one possible interpretation is the existence of an additional magnetic modulation in Phase I, where the magnetic structure can be described by the summation of a screw spin texture and a small amplitude of additional in-plane sinusoidal spin modulation. Such an anisotropic double-$\boldsymbol{Q}$ spin order for B = 0 has also been predicted by the theoretical model with RKKY and four-spin interactions [S1, S2] (In general, the energy gain by four-spin interaction can be finite when the summation of four relevant magnetic modulation vectors becomes zero. This is the reason why the triple-$\boldsymbol{Q}$ order with $\boldsymbol{Q}_1 + \boldsymbol{Q}_2 + \boldsymbol{Q}_3 = 0$ is often more favored under magnetic field with uniform magnetization component (i.e. $\boldsymbol{Q}_0 = 0$) on the triangular lattice. In principle, the double-$\boldsymbol{Q}$ order can be allowed even without uniform magnetization, and this may be the case for the present $GdRu_2Si_2$). Another possible interpretation is that the *B*–*T* region corresponding to Phase I may allow the co-existence of the transverse sinusoid component of Phase III. In this situation, Phase I is characterized by the long-range ordering of both in-plane and out-of-plane modulated spin component, while the coexisting transverse sinusoid state is characterized by long-range order of only the in-plane modulated spin component. Such partial magnetic order has often been observed in other noncollinear magnets with large thermal fluctuation [S3].

To conclude the detailed magnetic structure in Phase I, further experimental studies of both in-plane and out-of-plane spin components in real-space would be essential. Because this secondary peak disappears in Phases II and III, its presence in Phase I (B = 0 T) will not affect the discussion of skyrmion lattice formation, which is the main subject of this article.

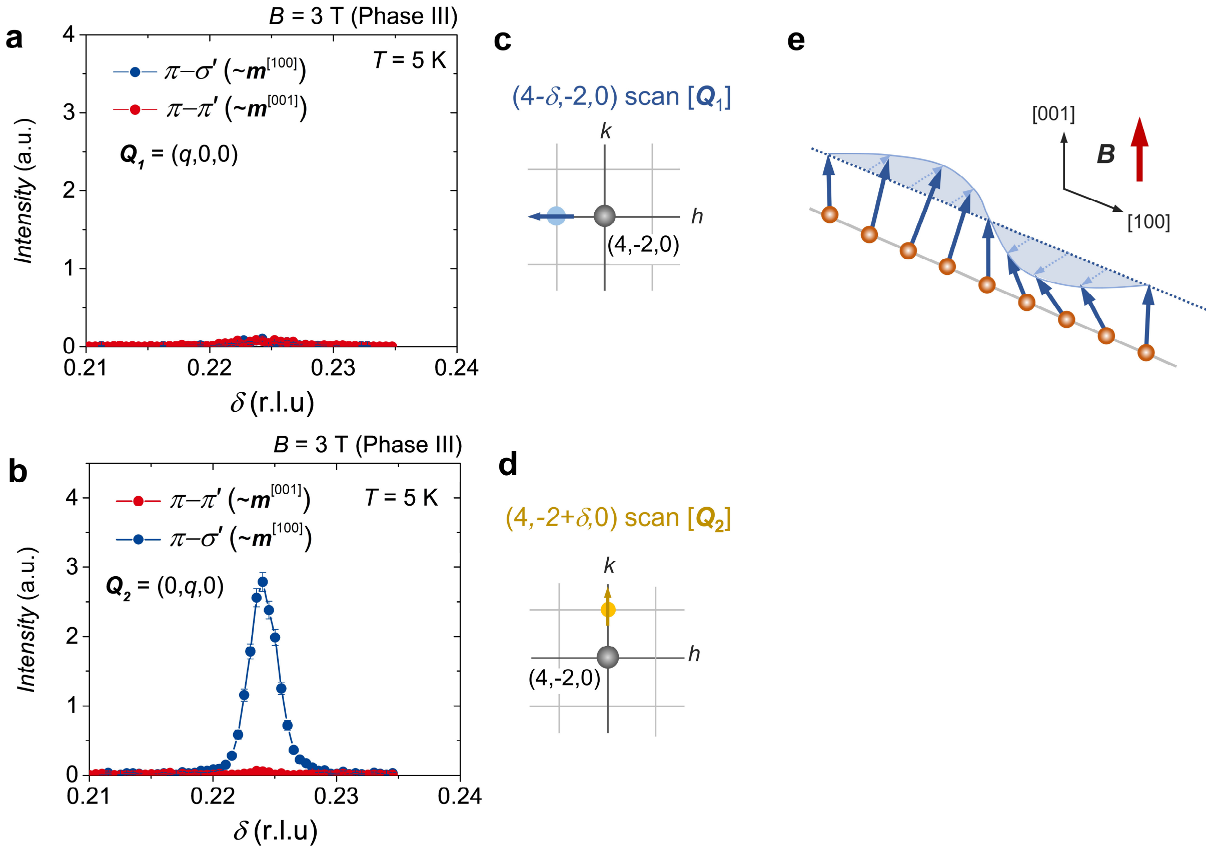

Supplementary Fig. 2 | Polarization analysis of RXS profiles in Phase III. Here, the same experimental geometry as shown in Figs. 3a and b in the main text is employed. **a**,**b**, Line scan profiles for (4-δ, -2, 0) and (4, -2+δ, 0), corresponding to $\boldsymbol{Q_1}$ and $\boldsymbol{Q_2}$, measured at 3 T in Phase III. **c**,**d**, Line-scan direction for $\boldsymbol{Q_1}$ and $\boldsymbol{Q_2}$ in reciprocal space. **e**, Real-space illustration of the fan-like spin structure with $\boldsymbol{Q_1}$ = (q, 0, 0) in Phase III. Error bars indicate one standard deviation.

III. Quantitative analysis of polarized RXS results

To further confirm the validity of the proposed magnetic structures, we performed additional polarized RXS experiments for the magnetic satellite peaks around the fundamental reflections (4, 0, 0) ± $\boldsymbol{Q}$ and (4, -2, 0) ± $\boldsymbol{Q}$. In Supplementary Fig. 3a (3b), we show theoretical and experimental values for the intensity ratios $I_{\pi\text{-}\sigma'}$ / $I_{\pi\text{-}\pi'}$ of various magnetic Bragg reflections. The theoretical values for the phase I were calculated based on Eq. (2) in the main text, assuming the single-$\boldsymbol{Q}$ proper-screw spin order. For the double-$\boldsymbol{Q}$ square skyrmion lattice order in phase II, we introduced small ellipticity in Eq. (4) as follows:

$$\boldsymbol{S}(\mathbf{r}) = \{(0, -iS_q^{xy}, S_q^z) \exp[i\boldsymbol{Q_1} \cdot \boldsymbol{r}] + (-iS_q^{xy}, 0, S_q^z) \exp[i\boldsymbol{Q_2} \cdot \boldsymbol{r}] + (0, 0, S_0^z)\} + c.c. \qquad \text{(S1)}$$

where $S_q^{xy} / S_q^z = 1.47$ and $S_0^z / S_q^z = -0.73$.

The corresponding experimental data were obtained at 0 T in Phase I and 2.1 T in Phase II, respectively. In both cases, the theoretical and experimental values are in quantitative agreement with each other, firmly establishing the validity of the proposed magnetic structures for Phases I and II.

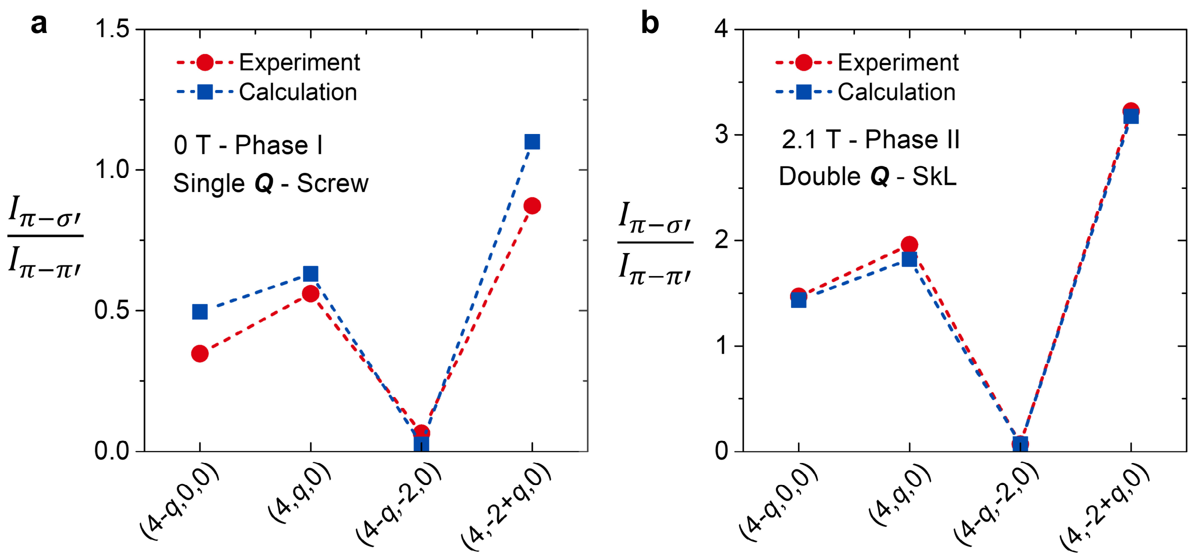

Supplementary Fig. 3 | a, Intensity ratios $I_{\pi\text{-}\sigma'}$ / $I_{\pi\text{-}\pi'}$ of various magnetic Bragg reflections obtained in polarized RXS measurement performed at 5 K and 0 T (Phase I). Theoretical values for the single-$\boldsymbol{Q}$ screw spin structure are also plotted. **b**, The corresponding experimental data at 2.1 T (Phase II) and theoretical values calculated for the double-$\boldsymbol{Q}$ square skyrmion lattice.

IV. Magnetic structure and topological number in Phase II

In the following, we discuss the magnetic structure and topological number of the double-$\boldsymbol{Q}$ magnetic order in Phase II. As demonstrated in the main text, the magnetic structure in Phase II can be roughly described by a superposition of two orthogonally-arranged screw spin textures with field-induced uniform out-of-plane magnetization component. When the two screw spin components with modulation vectors $\boldsymbol{Q_1} = (q, 0, 0)$ and $\boldsymbol{Q_2} = (0, q, 0)$ have the same helicity (Supplementary Figs. 4a and b), the magnetic structure $\boldsymbol{m}(\boldsymbol{r})$ can be described by Eq. (3) in the main text. The corresponding skyrmion number n_{sk} can be calculated based on Eq. (1) in the main text, and its dependence on the normalized magnetization M/M_0 induced by B // [001] is plotted in Supplementary Fig. 4d. Here, M_0 is saturated magnetization value and M/M_0 is given by

$$\frac{M}{M_0} = \int m_z(\boldsymbol{r}) d^2\boldsymbol{r} / \int d^2\boldsymbol{r} \,, \tag{S2}$$

where m_z is the [001] component of $\boldsymbol{m}(\boldsymbol{r})$ and the integral is taken over the two-dimensional magnetic unit cell. For moderate amplitude of M/M_0, the skyrmion number becomes n_{sk} = -1 (Supplementary Fig. 4d). Experimentally, Phase II in $GdRu_2Si_2$ corresponds to $M/M_0 \sim 0.37$ (Fig. 1f in the main text). The theoretical spin texture for $M/M_0 \sim 0.37$ (corresponding to $S_z = 0.70$ in Eq. (4)) is shown in Supplementary Fig. 4c, which can be considered as a square lattice of magnetic skyrmions. In this situation, the core-moments for the clockwise and counter-clockwise spin vortices are pointing along the opposite directions. At the middle point of the same-type of vortices, there are also anti-vortices whose core-moments are always pointing parallel to magnetic field. Therefore, the total skyrmion number is not canceled out, and non-zero integer skyrmion number $n_{\mathrm{sk}} = -1$ per magnetic unit cell can be obtained. This magnetic structure, described by Eq. (3) in the main text, is consistent with the one observed in the present LTEM experiments.

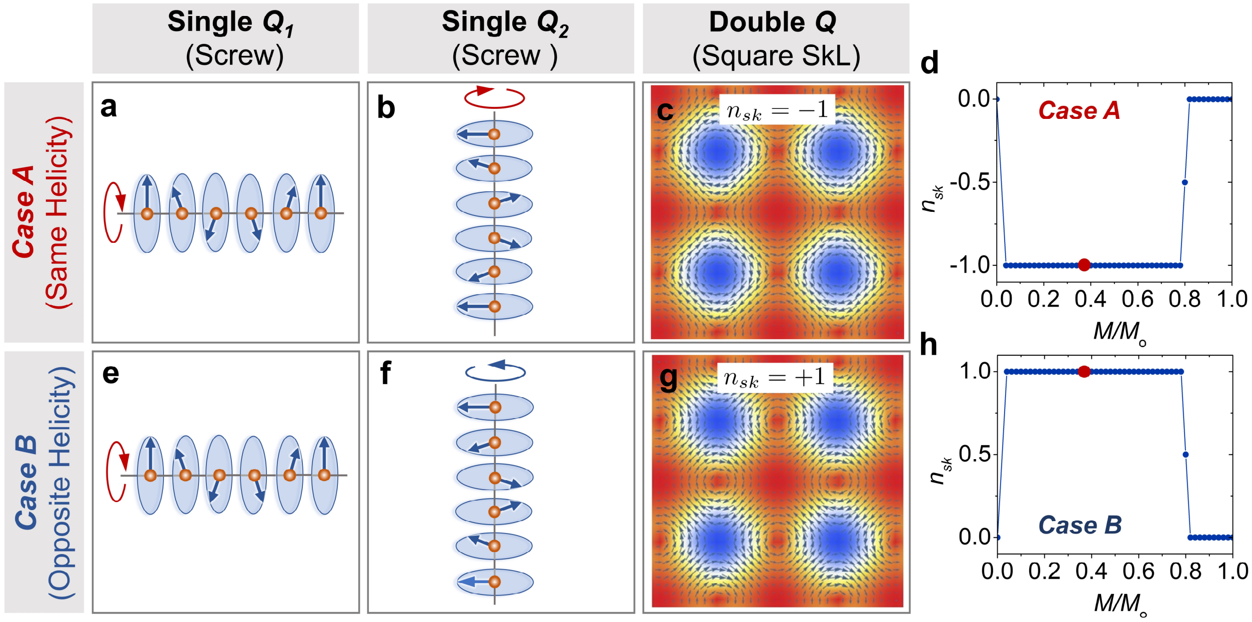

Supplementary Fig. 4 | **a**,**b**, Two orthogonally arranged screw spin structures with magnetic modulation vectors $\boldsymbol{Q}_1 = (q, 0, 0)$ and $\boldsymbol{Q}_2 = (0, q, 0)$, characterized by the same spin helicity. **c**, Double-$\boldsymbol{Q}$ square skyrmion lattice state deduced by the superposition of these two screw spin textures. **d**, Evolution of skyrmion number n_{sk} as a function of normalized magnetization M/M_0 induced by B // [001]. **e**-**h**, Corresponding figures for the case of two screw spin textures with opposite spin helicity.

When two orthogonally arranged screw spin components have opposite helicity as shown in Supplementary Figs. 4e and f, the associated double-$\boldsymbol{Q}$ magnetic structure can be described with

$$\boldsymbol{m}(\boldsymbol{r}) = \boldsymbol{S}(\boldsymbol{r}) / |\boldsymbol{S}(\boldsymbol{r})| \tag{S3}$$

$$\boldsymbol{S}(\mathbf{r}) = \{(0, -i, 1) \cdot \exp[i\boldsymbol{Q}_1 \cdot \boldsymbol{r}] + (-i, 0, 1) \cdot \exp[i\boldsymbol{Q}_2 \cdot \boldsymbol{r}] + (0, 0, S_z)\} + c.c. \tag{S4}$$

In this case, the skyrmion number becomes $n_{sk} = +1$ (Supplementary Fig. 4h) and the magnetic structure can be considered as a square lattice of antiskyrmions (Supplementary

Fig. 4g). The above two types of double-$\boldsymbol{Q}$ order can also be distinguished by a polarization analysis of the $\boldsymbol{Q}_1 + \boldsymbol{Q}_2$ magnetic reflection in RXS experiments as discussed below.

In Supplementary Fig. 5, we present polarized RXS data of the $\boldsymbol{Q}_1 + \boldsymbol{Q}_2$ magnetic satellite peak around the (4, 0, 0) fundamental reflection, taken at 5 K and $B = 2.1$ T applied parallel to the [001] axis (Phase II). Here, the incident X-ray wave vector $\boldsymbol{k}_i$ is almost parallel to [110] direction, while the scattering plane is perpendicular to the [001] axis as shown in Supplementary Fig. 5b. In this configuration, $I_{\pi\text{-}\pi'}$ and $I_{\pi\text{-}\sigma'}$ should mainly reflect the [001] and [110] components of $\boldsymbol{m}_{Q1+Q2}(\boldsymbol{r})$, respectively, according to Eq. (2) in the main text. As presented in Supplementary Fig. 5a, the experimentally observed $I_{\pi\text{-}\sigma'}$ is negligibly small as compared to $I_{\pi\text{-}\pi'}$, which indicates that $\boldsymbol{m}_{Q1+Q2}(\boldsymbol{r})$ does not have modulated spin component parallel to $\boldsymbol{Q}_1 + \boldsymbol{Q}_2$ // [110]. For the square lattice of skyrmion as shown in Supplementary Fig. 4c (anti-skyrmion as shown in Supplementary Fig. 4g), neighboring spins along the $\boldsymbol{Q}_1 + \boldsymbol{Q}_2$ // [110] direction rotate within a plane perpendicular (parallel) to $\boldsymbol{Q}_1 + \boldsymbol{Q}_2$, and therefore the component of $\boldsymbol{m}_{Q1+Q2}(\boldsymbol{r})$ parallel to $\boldsymbol{Q}_1 + \boldsymbol{Q}_2$ should be zero (non-zero). The observed absence of $I_{\pi\text{-}\sigma'}$ (i.e. the component of $\boldsymbol{m}_{Q1+Q2}(\boldsymbol{r})$ parallel to $\boldsymbol{Q}_1 + \boldsymbol{Q}_2$) in Supplementary Fig. 5a indicates that the square lattice of skyrmions as shown in Supplementary Fig. 4c is realized in Phase II for $GdRu_2Si_2$, consistent with the LTEM data in Fig. 4 of the main text.

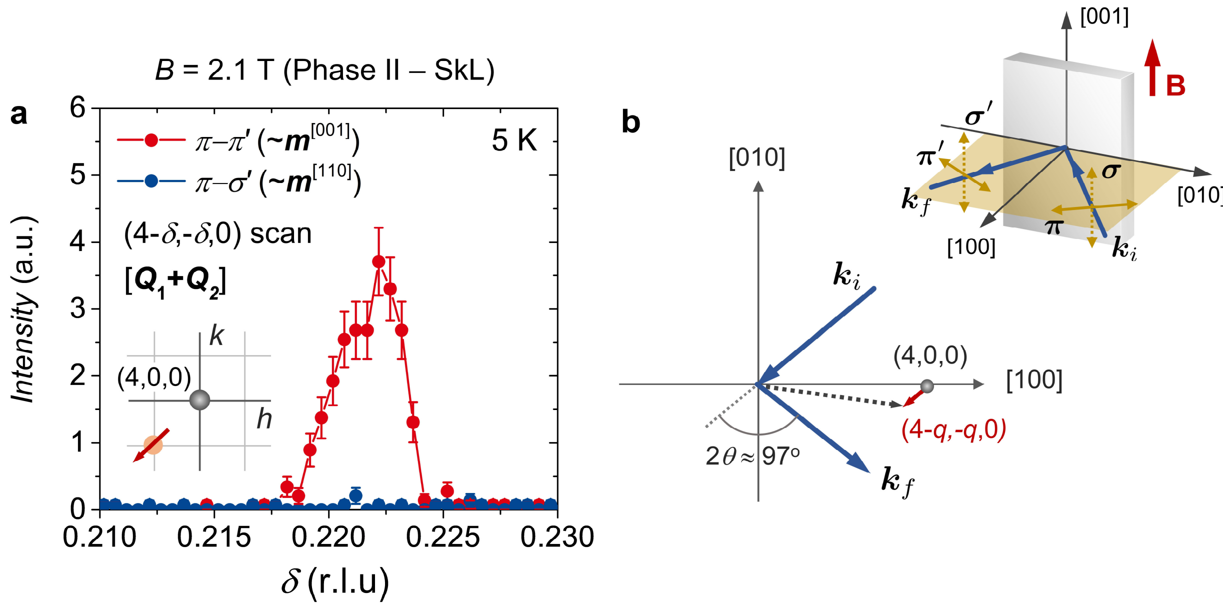

Supplementary Fig. 5 | Polarization analysis of RXS profile for the $\boldsymbol{Q_1} + \boldsymbol{Q_2}$ reflection in Phase II. **a**, Line scan profile for (4-δ, -δ, 0), which represents the $\boldsymbol{Q_1} + \boldsymbol{Q_2}$ modulation around (4, 0, 0) crystal Bragg spot at 5 K and 2.1 T (phase II). Here, intensities of π-π' and π-σ' channels mainly reflect the [001] and [110] components of $\boldsymbol{m}_Q(\mathbf{r})$, respectively. The corresponding experimental geometry is shown in (**b**). Error bars indicate one standard deviation.

V. Higher harmonics of magnetic modulation

As discussed in the main text, we assumed that the local amplitude of magnetic moment is fixed and doesn't depend on the position, because 4f magnetic moments on Gd^{3+} sites are localized. Here, the spin texture in the Phase II is approximately described by Eq. (3), which is not the simple superposition of harmonic helical spin texture but their local amplitude of magnetic moment is further normalized. As a result, the spin texture contains not only the fundamental harmonic component ($\boldsymbol{Q}_1$ and $\boldsymbol{Q}_2$) but also the higher harmonic component (such as $\boldsymbol{Q}_1 + \boldsymbol{Q}_2$, $2\boldsymbol{Q}_1$ and $2\boldsymbol{Q}_2$). These higher harmonic components can be directly detected by the resonant X-ray scattering measurements. In this section, we mainly discuss the experimental detection of $2\boldsymbol{Q}_1$ component (The detailed discussion on the $\boldsymbol{Q}_1 + \boldsymbol{Q}_2$ modulation component is also provided in Figure 2 and Supplementary Fig. 5 and the associated text).

Supplementary Figs. 6a and b indicate the (4-δ, 0, 0) line scan profiles measured at 2.15 T (i.e. in the Phase II (square SkL state)), representing the $\boldsymbol{Q}_1$ and $2\boldsymbol{Q}_1$ magnetic satellite peaks around fundamental Bragg position (4,0,0), respectively. Here, the ratio between the integrated intensity of $2\boldsymbol{Q}_1$ and $\boldsymbol{Q}_1$ reflections (I_{2Q_1}/I_{Q_1}) is approximately 1%. Since the intensity of magnetic scattering is basically proportional to square of $\boldsymbol{m_Q}$ according to Eq. (2) in the main text, the relative amplitude of the second harmonics in the spin texture can be estimated as an order of $|\boldsymbol{m}_{2\boldsymbol{Q}_1}|/|\boldsymbol{m}_{\boldsymbol{Q}_1}| \sim \sqrt{I_{2Q_1}/I_{Q_1}} \sim 10\%$. (Note that the above discussion allows only a rough estimate of the order of higher harmonics. For the detailed quantitative analysis, we also have to consider the polarization of the incident and scattered beam as well as the associated selection rule given by Eq. (2).) In Supplementary Figs. 6c-e, magnetic field dependence of I_{2Q_1}, I_{Q_1} and $\sqrt{I_{2Q_1}/I_{Q_1}}$ ($\sim |\boldsymbol{m}_{2\boldsymbol{Q}_1}|/|\boldsymbol{m}_{\boldsymbol{Q}_1}|$) are also plotted.

As shown in Fig. 2d and f in the main text, the ratio between the integrated intensity of $\boldsymbol{Q}_1 + \boldsymbol{Q}_2$ and $\boldsymbol{Q}_1$ reflections ($I_{Q_1+Q_2}/I_{Q_1}$) in the Phase II is found to be as large as 10%, which implies that the Phase II is characterized by even larger amplitude of $\boldsymbol{Q}_1 + \boldsymbol{Q}_2$ component in addition to the $2\boldsymbol{Q}_1$ (and equivalent $2\boldsymbol{Q}_2$) component.

Note that in the present manuscript, the term "double-$\boldsymbol{Q}$", "triple-$\boldsymbol{Q}$" or "multiple-$\boldsymbol{Q}$" is used just to describe the number of coexisting fundamental modulation vectors in the target spin texture, and it does not mean the absence of higher harmonic components. As discussed in Ref. [S4], the simple superposition of harmonic helical spin texture leads to the spatially variant amplitude of local magnetic moment, and therefore the further consideration of higher harmonic components (as experimentally detected in the above) is essential to resolve the spin texture in the SkL state. In the current work, we naively assumed that the spin texture in the Phase II can be approximately described by Eq. (3), while the actual spin texture stabilized in $GdRu_2Si_2$ (i.e. the relative amplitude of higher harmonics, in particular) is probably slightly different from this model. Nevertheless, we believe that Eq. (3) still captures the overall qualitative feature of spin texture in Phase II, especially in terms of the magnetic symmetry and skyrmion number.

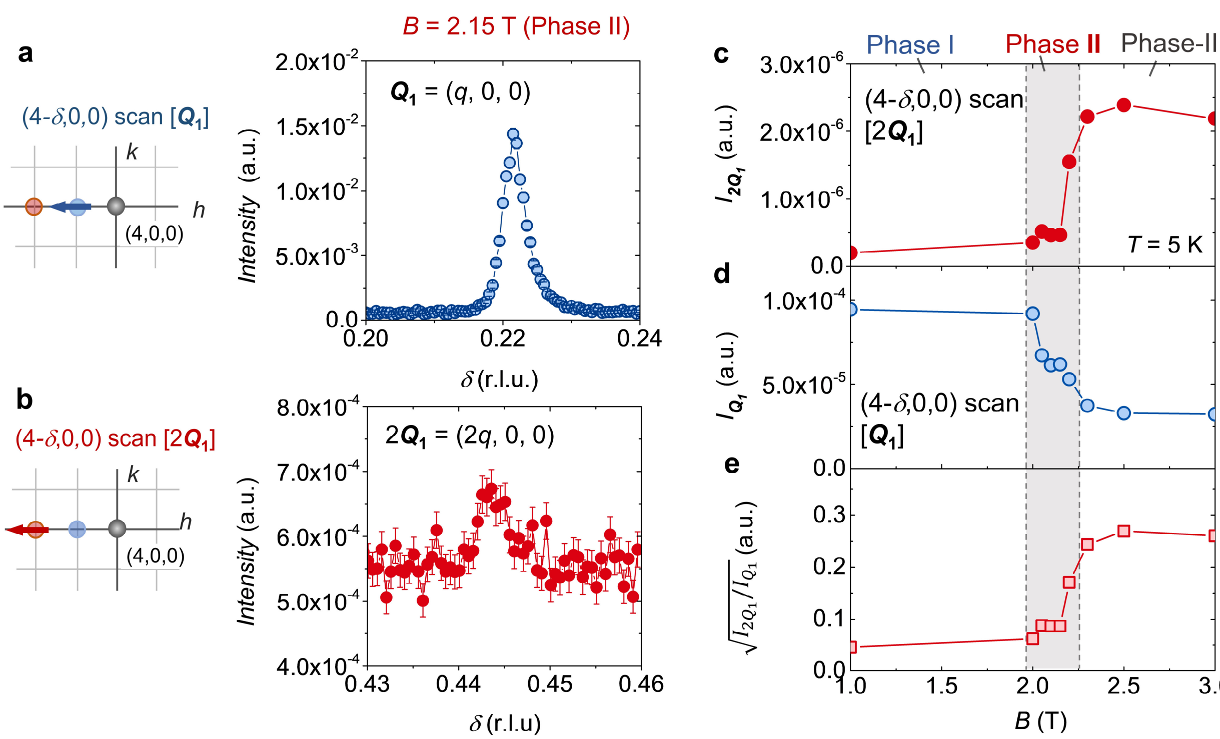

Supplementary Fig. 6 | a,**b**, The line scan profiles for (4-δ,0,0) scans, corresponding to $\boldsymbol{Q}_1$ and 2$\boldsymbol{Q}_1$ magnetic satellite peaks around the fundamental Bragg spot (4,0,0) in phase II (B = 2.15T), respectively. Line scan direction is depicted on the left side of each figure. **c**-**e**, Magnetic field dependence of integrated intensity of 2$\boldsymbol{Q}_1$ and $\boldsymbol{Q}_1$ reflections (I_{2Q_1} and I_{Q_1}, respectively) and $\sqrt{I_{2Q_1}/I_{Q_1}}$. Error bars indicate one standard deviation.

VI. Hall resistivity data

In this part, we discuss the electrical transport properties associated with the formation of the square skyrmion lattice in Phase II. In Supplementary Fig. 7a, the ρ_{yx}-B profiles measured at various temperatures are plotted. The prominent enhancement of $|\rho_{yx}|$ is always observed upon the transition into Phase II as discussed for Fig. 1 in the main text, whose amplitude is gradually suppressed for higher temperature and finally disappears above 25 K. Supplementary Fig. 7b summarizes the *B*-*T* magnetic phase diagram for *B* // [001]. The anomalies in *M*, ρ_{xx}, and ρ_{yx} profiles always coincide with each other, demonstrating the strong correlation between magnetism and transport properties in $GdRu_2Si_2$.

In general, the Hall resistivity $\rho_{yx} = \rho_{yx}^N + \rho_{yx}^A + \rho_{yx}^T$ is described as the summation of normal Hall resistivity $\rho_{yx}^N = R_0 B$ proportional to B, anomalous Hall resistivity $\rho_{yx}^A = R_S M$ proportional to *M*, and topological Hall resistivity $\rho_{yx}^T = P R_0 B_{eff}$ proportional to the emergent magnetic field B_{eff}. Here, *P* is the spin-polarization ratio of the conduction electron, and R_0 and R_s are normal and anomalous Hall coefficients, respectively. In the continuum approximation, the emergent magnetic field associated with the quantum Berry phase gained by conduction electrons passing through the skyrmion spin texture is given by $B_{eff} = \Phi_0 \Phi$, with Φ and $\Phi_0 = h/e$ representing skyrmion density and flux quantum. If we naively assume that the observed prominence of $|\Delta\rho_{yx}| \sim 0.1\ \mu\Omega$cm in Phase II would purely originate from ρ_{yx}^T and the continnum approximation would be still valid for nanometric SkL with short modulation period ~1.9 nm, B_{eff}^z ~ 600 T and *P* ~ -0.03 are obtained (*P* = 0.07 and *P* = 0.01 ~ 0.05 have been proposed for Gd_2PdSi_3 [S5] and $Gd_3Ru_4Al_{12}$ [S6], respectively). In reality, however, the non-monotonous magnetoresistance and large anomalous Hall angle (Figs. 1g and h in the main text) implies that the anomalous Hall coefficient R_S may also show complex B-dependence, depending on its microscopic mechanism [S7], and the very short modulation period of magnetic texture comparable to a few times of lattice spacing may compromise the validity of continuum approximation. For the complete understanding of the observed ρ_{yx} profile and quantitative evaluation of ρ_{yx}^T, further theoretical and experimental investigations would be required.

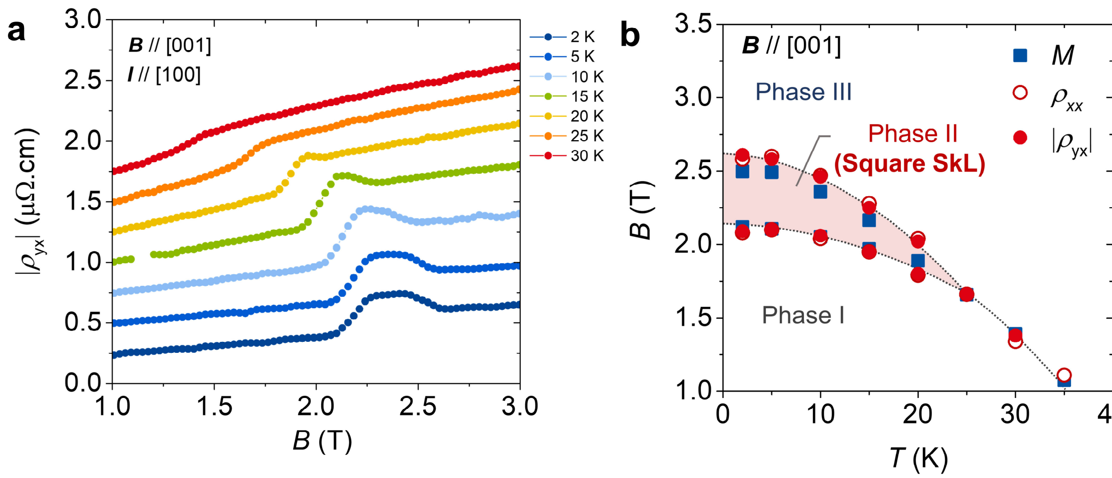

Supplementary Fig. 7 | Hall resistivity profiles for $GdRu_2Si_2$. **a**, Magnetic-field dependence of Hall resistivity ρ_{yx} measured at various temperatures (Data at 1T are shifted 0.25 μΩ.cm to each other). **b**, Magnetic phase diagram for ***B*** // [001], based on the anomalies in the *M*, ρ_{xx} and ρ_{yx} profiles.

VII. Energy dependence of magnetic X-ray scattering

In Supplementary Fig. 8, we present the photon-energy dependence of the magnetic Bragg reflection (4-δ, 0, 0) with $\delta = 0.22$ in the X-ray scattering experiment. A resonance peak was observed at the Gd L_2 absorption edge at 7.935 keV, which corresponds to the transitions from 2*p* core states to the 5*d* states of Gd. This confirms that the RXS results indeed reflect the magnetic properties of the Gd site in $GdRu_2Si_2$.

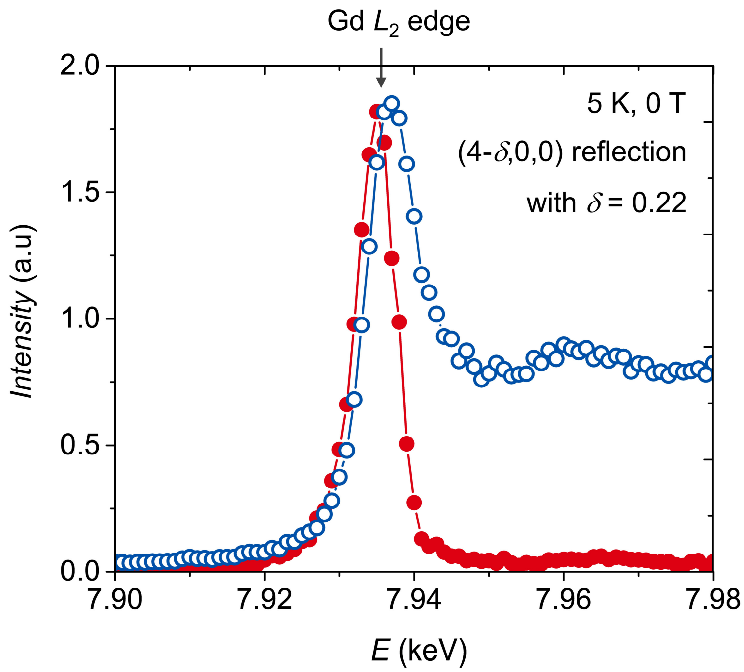

Supplementary Fig. 8 | Solid red symbols show the energy dependence of the scattering intensity of the (4-δ, 0, 0) magnetic X-ray reflection with $\delta \sim 0.22$ measured at 5 K and 0 T. Blue symbols are the excitation spectrum of X-ray fluorescence.

VIII. The choice of Bragg positions for resonant X-ray scattering experiments

In the following, we explain the reason to choose each Bragg position for resonant X-ray scattering experiments.

The reason to select (4, 0, 0) fundamental reflection is that the signal-to-noise (S/N) ratio for the magnetic scatterings is the highest near this reflection, where the 2θ angle is close to 90^{o}. In order to have highest S/N, which is required measure the $\boldsymbol{Q}_1 + \boldsymbol{Q}_2$ reflection, we need to minimize the contribution from noise and background.

In particular, the background signals are mainly charge scatterings from the sample holder, windows of the magnet, helium gas, etc. and the X-ray fluorescence. The *non-resonant charge scattering intensity* (which causes undesired signals) is proportional to

$(\boldsymbol{e}_i . \boldsymbol{e}_f)^2$, with $\boldsymbol{e}_i$ and $\boldsymbol{e}_f$ representing the polarization vectors of incident and scattered beams, respectively. At the instrument where the present experiment was performed (BL3A, PF-KEK), we used the π-polarized incident X-ray, and the scattering plane is horizontal (as shown schematically in Figure 3a in the main text and Supplementary Fig. 5b). Therefore, the factor $(\boldsymbol{e}_i . \boldsymbol{e}_f)^2$ is minimized (to zero in an ideal case) when $\boldsymbol{e}_i$ and $\boldsymbol{e}_f$ are perpendicular to each other, that is, the configuration corresponding to (4, 0, 0) reflection with $2\theta \approx 90^{\circ}$. In addition, to identify the exact position of $\boldsymbol{Q}_1 + \boldsymbol{Q}_2$, we also need to precisely determine the peak positions of $\boldsymbol{Q}_1$ and $\boldsymbol{Q}_2$, which can be achieved more convenient in (4, 0, 0) reflection comparing with (4, -2, 0) one.

For the polarization analysis, on the other hand, the magnetic satellite reflections near the reciprocal lattice point of (4, -2, 0) is more suitable. Here, our main purpose is to distinguish the Neel (cycloid) and Bloch (screw) type magnetic modulations; the former has modulated spin components parallel to the $\boldsymbol{Q}$-vector, but the latter does not. When measuring a satellite reflection at (4-q, -2, 0) with the π-σ' configuration, $\boldsymbol{e}_i$ is almost parallel to the [010] axis, and $\boldsymbol{e}_f$ is parallel to [001] by definition. By substituting these conditions into Eq. (2), one can find that the $I_{\pi\text{-}\sigma'}$ for this reflection is proportional to the modulated spin component parallel to the $\boldsymbol{Q}$-vector. The absence of π-σ' scattering at (4-q, -2, 0), which is shown in Figs. 3c and d in the main text, clearly indicates that the magnetic modulations in the phase I and II are the screw (Bloch) type.

References

[S1] Ozawa, R. *et al.* Vortex crystals with chiral stripes in itinerant magnets. *J. Phys. Soc. Jpn.* **85**, 103703 (2016).

[S2] Hayami, S., Ozawa, R. & Motome, Y. Effective bilinear-biquadratic model for noncoplanar ordering in itinerant magnets. *Phys. Rev. B* **95**, 224424 (2017).

[S3] Mitsuda, S. *et al.* Partially Disordered Phase in Frustrated Triangular Lattice Antiferromagnet $CuFeO_2$, *J. Phys. Soc. Jpn.* **67**, 4026 (1998).

[S4] Rößler, U. K. *et al.*, Chiral skyrmionic matter in non-centrosymmetric magnets, *J. Phys. Conf. Ser* **303**, 012105 (2011).

[S5] Kurumaji, T. *et al.* Skyrmion lattice with a giant topological Hall effect in a frustrated triangular-lattice magnet. *Science* **365**, 914-918 (2019).

[S6] Hirschberger, M. *et al*. Skyrmion phase and competing magnetic orders on a breathing kagomé lattice, *Nat*. *Commun.* **10**, 5831(2019).

[S7] Nagaosa, N. *et al.* Anomalous Hall effect, *Rev. Mod. Phys.* **82**, 1539 (2010).